Development and Optimization of a VUV Laser Alignment System for Antihydrogen Cooling in the ALPHA Experiment

Firas Batwa
Under the Supervision of Andrew Evans
In Collaboration with Aryan Prasad

August, 2025

Abstract

This report presents the development and optimization of a vacuum ultraviolet (VUV) laser alignment system for antihydrogen cooling within the ALPHA experiment at CERN. To enable Doppler laser cooling at 121.6 nm via the 1S–2Pf transition, a third-harmonic generation process is employed to produce Lyman-alpha radiation from a 365 nm input laser. Optical alignment is the most challenging step; our goal is to automate it and maximize the spatial separation between the 121.6 nm and 365 nm beams, thereby improving the stability and efficiency of the nonlinear conversion. This project involved surveying the existing optical system, implementing a ray-tracing model using Optiland, and optimizing beam separation and focusing by adjusting the mirror angles. In parallel, a detailed characterization of the picomotor-driven mirrors was performed, revealing nonlinearities and hysteresis that pose challenges for automation. Feedback-based solutions were explored, but were hindered by hardware limitations. As an alternative, a passive alignment system using irises on translation stages was proposed and integrated. The resulting methodology enhances reproducibility and streamlines the alignment process, laying the groundwork for the future implementation of a closed-loop optimization system.

Contents

Introduction

What is Antimatter?

In 1928, Paul Dirac predicted the existence of antimatter as a mathematical consequence of combining quantum mechanics and special relativity through the Dirac equation. A few years later, in 1932, the first observation of antimatter was detected through cosmic ray experiments.

Antimatter refers to a family of particles that have the same mass as their counterparts in ordinary matter but opposite charge. For example, a positron has the same mass as an electron but a positive charge.

The contact of matter and antimatter leads to annihilation—a highly energetic reaction in which the rest mass of both particles is converted into new particles. For example, when an electron and a positron meet, $e^- + e^+ \to 2\gamma$, the result is two photons. In contrast, the annihilation of a proton and an antiproton, $p + \bar{p} \to \pi^0 + \pi^- + \pi^+$, typically produces several pions. These pions are unstable: neutral pions decay to photons ($\pi^0 \to \gamma\gamma$), while charged pions decay to muons and neutrinos ($\pi^\pm \to \mu^\pm \nu$). Thus, annihilation channels ultimately yield photons and leptons, which carry away the released energy.

In the Standard Model, symmetry between matter and antimatter implies that the Big Bang should have created them in nearly equal amounts; if that were true, almost all pairs would have annihilated away. Yet observations, especially of the cosmic microwave background and the large-scale distribution of galaxies, show a universe dominated by matter. This "matter–antimatter asymmetry" (also called the baryon asymmetry) remains one of the outstanding puzzles in physics [1].

Technical Background

Antimatter Production at CERN

Since antiparticles are not readily found on Earth, scientists studying antiparticles must create the particles themselves. Antiprotons are made by first accelerating regular protons to very high energies on the order of GeV. CERN accomplishes this using a series of accelerators, starting with LINAC-2, followed by the Proton Synchrotron Booster, and finally the Proton Synchrotron (PS) [2].

These accelerated protons are then smashed into an iridium target. When protons collide with the target nuclei, the collision produces a cascade of secondary particles through a process known as pair production. These reactions cause energy to be converted into mass, creating proton–antiproton pairs among other particles.

Although many protons collide with the iridium nuclei, only a small fraction of antiprotons are made, and they are usually scattered in a wide range of angles and energies, so magnetic lenses are used to separate the antiprotons from the rest of the collision debris.

These antiprotons are typically moving too fast to study using atomic physics techniques, so CERN implements an antiproton decelerator (AD) to reduce their energy from 3.5 GeV to about 5.3 MeV [2]. For even lower energy experiments, the ELENA ring (Extra Low Energy Antiproton facility) further cools and slows them down to approximately 100 keV [3]. After being significantly slowed, these antiprotons can be trapped using Penning traps, which suspend them in strong electromagnetic fields so that the antiprotons do not annihilate when they come into contact with protons.

ALPHA (Antihydrogen Laser Physics Apparatus)

The ALPHA collaboration operates at CERN's AD. It focuses on the production, confinement, and high-precision spectroscopic and gravitational interrogation of antihydrogen [4, 5]. Antihydrogen is a bound state of an antiproton and a positron. By exploiting the well-understood nature of the hydrogen atom, ALPHA's primary objective is to test CPT invariance by comparing the fundamental spectral and gravitational features of antihydrogen with those of hydrogen [5]. Any deviation from spectral lines, such as the 1S–2S transition or the Lamb shift, could signal physics beyond the Standard Model and provide insight into the observed baryon asymmetry of the universe [6].

ALPHA accumulates positrons in a Surko-type accumulator. These particles, together with antiprotons from the AD, are highly energetic and must be cooled in nested Penning traps before mixing. The traps use a strong magnetic field and a series of electrodes set to different voltages to create electrostatic potential wells [4, 7]. These voltage wells allow the charged particles to be confined axially, while the magnetic field confines them radially. Because of this setup, particles undergo cyclotron motion—a circular trajectory caused by the Lorentz force acting on the charged particles in the magnetic field. This motion plays a crucial role in confinement and is essential for cooling and compression techniques, such as rotating wall compression [4].

Additionally, the positron plasma is sympathetically cooled by laser-cooled Be^+ ions co-trapped in the Penning trap. Through Coulomb coupling, energy is transferred from the positrons to the cold ions, lowering the positron temperature without any material contact—thereby avoiding annihilation while enabling efficient cooling.

By carefully shaping the voltage profile, the positron and antiproton clouds can be brought into overlap, a process essential for the formation of antihydrogen.

ALPHA forms antihydrogen via three-body recombination ($e^+ + e^+ + \bar{p} \to \bar{H} + e^+$). One positron binds to the antiproton while the second carries away the excess energy and momentum. A single positron and antiproton pair cannot radiate energy quickly enough to bind on its own. Under our cryogenic plasma conditions, this mechanism preferentially produces the coldest antiatoms [8].

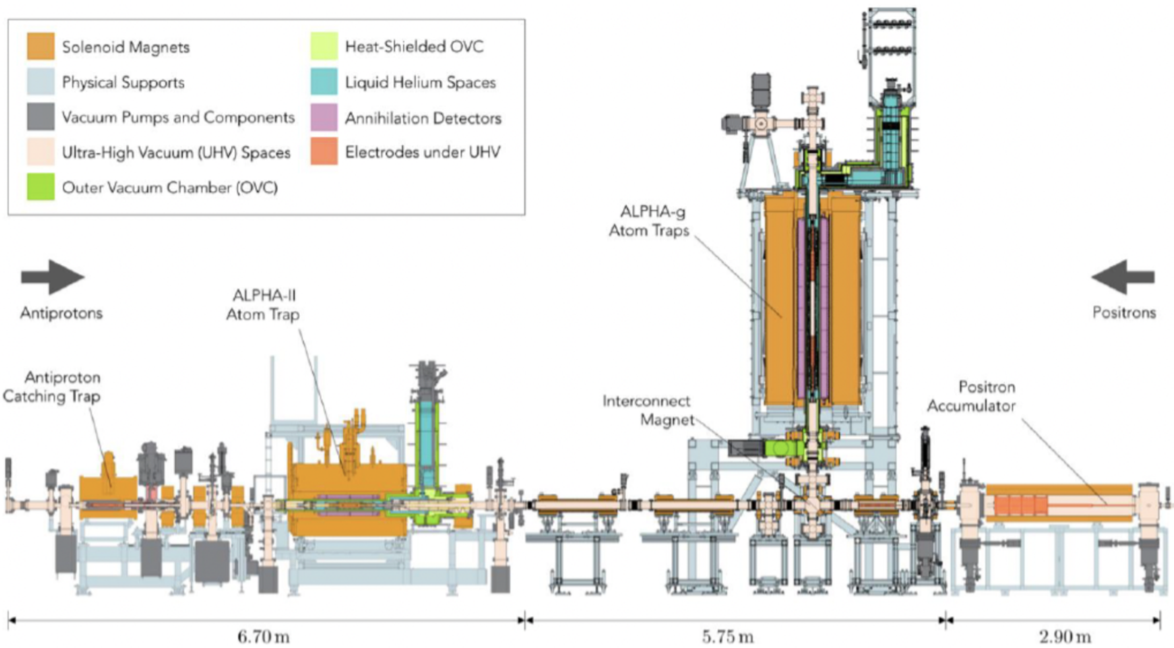

Figure 1: Schematic of the ALPHA-2 and ALPHA-g apparatus. Antiprotons from the AD facility enter from the bottom and are captured in the Catching Trap (CT), where they are cooled before being transferred to the ALPHA-2 Atom Trap (AT). Positrons, prepared in the positron accumulator (POS), are also sent to the AT. In the AT's minimum-B trap, the two species combine to form antihydrogen. ALPHA-g and its connecting beamline enable measurements of antihydrogen's gravitational behavior. Figure credit: Mark Johnson.

Once formed, the neutral antiatoms are no longer influenced by the electric fields of the Penning trap. Instead, they are confined in a minimum-B magnetic trap, created using a combination of axial mirror coils and radial octupole fields.

Laser Cooling

To cool these trapped antihydrogen atoms, ALPHA uses a VUV laser to drive the 1S–2Pf Lyman-alpha transition at 121.6 nm [9]. This transition is ideal because it is a strong, single-photon line directly from the ground state, allowing atoms to repeatedly absorb and emit without being lost to other states [10]. Although 121.6 nm photons carry relatively large recoil momentum—which is not, by itself, favorable for deep cooling—the line's strength and short excited-state lifetime make it the practical choice for antihydrogen cooling [11].

This is the simplest laser-cooling mechanism and works through the Doppler effect. If an atom moves toward the incoming beam, the light is Doppler-shifted to a higher frequency in the atom's rest frame. By tuning the laser slightly below resonance, those atoms preferentially absorb photons and receive momentum kicks opposite their motion [10]. Their kinetic energy decreases, and the sample cools. Atoms moving away see the light shifted to lower frequencies, further from resonance, and are less likely to absorb; in this way, the laser narrows the velocity distribution and lowers the overall temperature.

Producing the light needed for this in antihydrogen requires a complex and volatile laser system. In general, a laser works by exciting a gain medium, a material whose atoms can be stimulated to emit light at a specific wavelength, using an external energy source. This light is amplified between two mirrors that form an optical cavity, where it bounces back and forth, stimulating more atoms to emit photons of the same wavelength and phase. A small portion of the light is allowed to escape the cavity as the laser beam. Generating 121.6 nm light is technically challenging; the dedicated Lyman-alpha laser system (next section) produces it via resonantly enhanced third-harmonic generation in a Krypton/Argon gas cell [11].

By reducing the velocity spread of the trapped antihydrogen, laser cooling significantly improves the precision of measurements. This laser system also allows for time-of-flight profiles, making it easier to track the motion of the atoms, while spectral linewidths narrow due to reduced Doppler broadening. Overall, cooler antihydrogen samples lead to a more accurate determination of transition frequencies, enhancing both spectroscopic studies and gravitational measurements in experiments.

Lyman-alpha Laser System

Producing light at 121.6 nm for the 1S–2Pf transition is nontrivial due to the lack of available gain media and optical components at short wavelengths. ALPHA overcomes this limitation by employing a nonlinear resonantly enhanced third-harmonic generation (THG) in a krypton/argon (Kr/Ar) gas cell, utilizing a pulsed VUV laser system [12].

The process begins with a 730 nm continuous-wave (CW) seed laser, which is temporally shaped and amplified into nanosecond-scale pulses using a Ti:sapphire-based enhancement cavity pumped by a 532 nm Nd:YAG pulsed laser. These 730 nm pulses undergo second-harmonic generation (SHG) in a beta-barium borate (BBO) nonlinear crystal, producing 365 nm light. The 730 nm and 365 nm beams are then co-focused into a pressurized Kr/Ar gas cell, where they drive a resonantly enhanced THG process. This THG ($\omega + \omega + \omega \rightarrow 3\omega$) in the Kr/Ar mixture efficiently produces light at 121.6 nm (i.e., the third harmonic of 365 nm), corresponding precisely to the Lyman-alpha transition [12].

Project Overview

The optical alignment system for the laser splitting setup comprises three steering mirrors and two focusing lenses, with a Kr/Ar gas cell positioned between the lenses to facilitate nonlinear frequency conversion. An iris is placed downstream to selectively block the 365 nm beam while allowing the 121.6 nm Lyman-alpha light to pass through. Mirror A and Mirror C are mounted on picomotor stages, which are not used in the current alignment procedure.

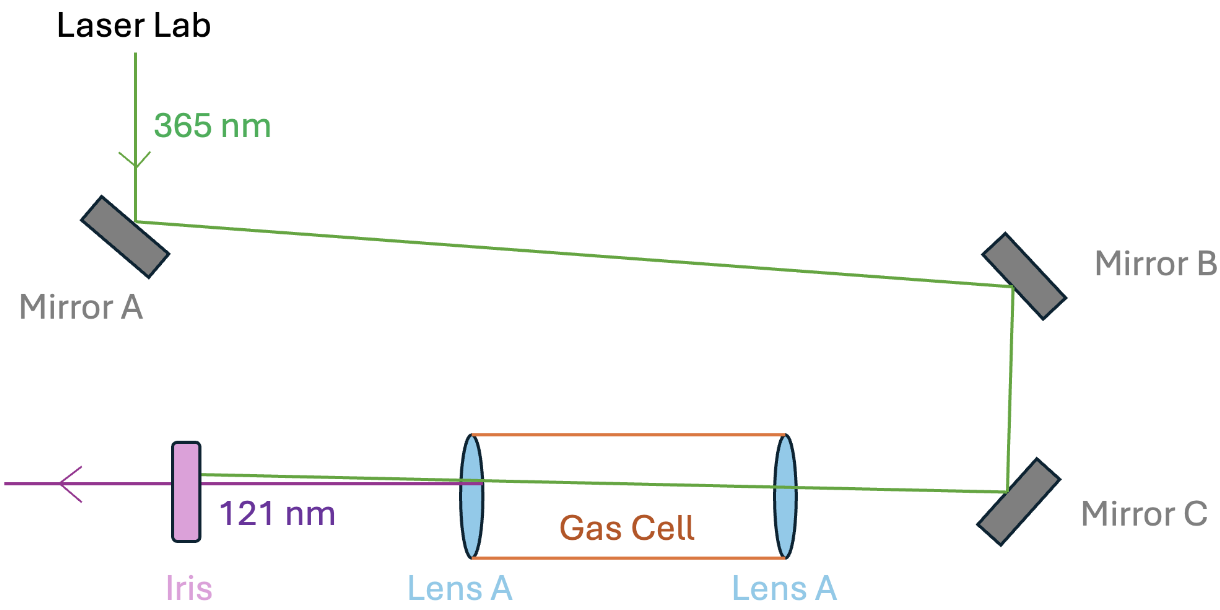

Figure 2: Optical layout for generating 121.6 nm light from a 365 nm laser using a gas cell and focusing optics.

To align the laser path, my mentor, Andrew Evans, employed a visible violet alignment laser as a reference beam. This beam was introduced at the end of the optical system to define a central optical axis. A piece of paper with a ruler was placed immediately after the third mirror to observe and compare the beam spots of both the violet alignment laser and the 365 nm UV beam. Alignment was refined until both beams struck the same point on opposite sides of the paper, confirming collinearity. This process is repeated at two locations along the optical paths.

After initial alignment, a deliberate transverse offset of approximately 4 mm was introduced between the 365 nm and violet beams using precision mirror adjustments. A similar spatial offset was applied to the 365 nm laser before the first mirror. The mirrors were then iteratively adjusted to optimize the beam splitting and focusing conditions through the gas-cell medium.

Verification of successful 121.6 nm generation was performed using a photodetector signal monitored on an oscilloscope. The appearance of distinct peaks corresponding to the VUV pulse confirmed that frequency tripling had occurred. The signal is confirmed to be 121.6 nm light by pumping out the THG gas cell. This alignment process is inherently challenging due to the extreme sensitivity of 121.6 nm light to beam path deviations and optical losses, as well as the requirement for careful spatial separation between the 365 nm and 121.6 nm beams to prevent cross-contamination. All of this is confounded by the lack of access to the optical system, as it is in a vacuum system.

To improve the reproducibility and efficiency of the alignment process, I collaborated with Aryan Prasad to develop an optimized method for aligning the optical system. Our work focused on identifying key beam path parameters that maximize third harmonic output separation and proposing a streamlined calibration protocol to reduce alignment time and enhance system stability in future experimental runs. Initially, we aimed to integrate picomotor-controlled mirrors with an optical optimization algorithm capable of determining the ideal beam path and automatically adjusting the mirror positions accordingly. With the target geometry defined, we surveyed the as-built system to parameterize the model.

Experimental Setup

The first step of the project involved surveying the optical system. These measurements will serve as input parameters for the optimization code being developed to improve the alignment and performance of the laser system. To complete the survey, we entered the designated zone of the ALPHA apparatus and manually measured the distances between the centers of each optical component using a ruler and laser range finder. We report a distance uncertainty of ±1 cm. This comes from three independent effects in our survey: reading and placing the ruler introduces about 2–3 mm, identifying each optic's center by eye contributes roughly 4–6 mm, and the laser rangefinder's stated accuracy in our geometry is about 2–3 mm. Treating these as random and adding them in quadrature gives $\sqrt{3^2 + 6^2 + 3^2} \approx$ 7–9 mm. We round this to a conservative ±1 cm to also cover minor systematics (parallax, slight misleveling, or table drift) that are hard to quantify but small compared to this budget.

Table 1: Baseline Optical Path Survey for VUV Generation Setup

Component/Section	**Details**
Beam Entry Point	Enters at Mirror A
Mirror A to Mirror B	Distance: 118–119 cm (center optics, free air)
Mirror B	Flat mirror, Diameter: 2.5 cm
Mirror B to Mirror C	Distance: 13–14 cm (free space)
Mirror C	Flat mirror, Diameter: 2.5 cm
Mirror C to Lens A	Distance: 10 cm
Lens A	Focal Length: 300 mm
Lens A to Lens B	Distance: 48 cm (enclosing gas cell) Gas Type: Argon/Krypton Gas Pressure: ∼2300 ± 1 Torr
Lens B	Focal Length: 150 mm
Lens B to Iris	Distance: 96 cm

Optical Modeling and Optimization

To model and optimize the beam path of our optical system, we utilized `Optiland`, a Python-based ray-tracing and optical design package. `Optiland` provides a programmable framework for simulating the propagation of light through a system of lenses, mirrors, apertures, and materials. It also supports performance analysis and optimization through built-in utilities such as spot diagrams and multi-variable optimization routines.

We implemented a detailed model of our experimental setup in Python, replicating the physical positions, angles, and materials of the components measured during our initial optical survey. The model comprises 15 surfaces representing various elements in the system, including steering mirrors, a gas cell, two lenses, and several apertures. The laser beam is traced from the source, reflected off three steering mirrors, passes through focusing lenses and the nonlinear gas medium, and terminates at the image plane.

System Components and Materials

Key optical components were defined using `Optiland` 's `optic.Optic` class. Mirrors were modeled with adjustable tilt angles to simulate fine-tuning of beam direction. Two lenses were placed before and after the gas cell, and the refractive properties of the materials were assigned based on empirical data. Three materials were used:

- UV Fused Silica for the 365 nm input beam
- Argon (approximating Kr/Ar mixture), loaded from a `.yml` file, as the nonlinear medium
- Magnesium Fluoride (MgF_2), also from a `.yml` file, for the final focusing lens

The beam was modeled at two wavelengths: 365 nm (input) and 121.6 nm (output, Lyman-alpha), both of which were traced simultaneously to analyze separation and focusing.

Spot Diagram Analysis

`Optiland`'s `SpotDiagram` module was used to quantify optical performance. The spot diagram calculates the spatial spread of rays at the image plane and determines key metrics such as the geometric spot radius and beam centroid. The primary metric of interest was the separation between the centroids of the 365 nm and 121.6 nm beams at the output. A well-aligned system should exhibit significant centroid separation and small spot sizes. Large centroid separation cleanly distinguishes the 365 nm and 121.6 nm beams, while small spot sizes indicate low aberrations and high-throughput alignment.

We defined a custom function, `sep_ratio(system)`, to compute the ratio between the centroid separation and the geometric spot radius, serving as the primary operand in the optimization process to maximize beam separation.

Optimization Strategy

To improve the system alignment, we used Optiland's optimization module. An `OptimizationProblem` object was initialized with two main operands:

- Centroid Separation Ratio: the distance between the 365 nm and 121.6 nm spot centers divided by the larger spot's size; we maximize it so the beams are well separated relative to their size and therefore easy to distinguish.
- Beam Alignment: Constrained the final beam location to lie near the desired image plane to ensure physical feasibility.

We optimized the tilt angles of mirrors A and C, allowing each variable to vary within a defined angular range (up to $\pm 90°$). The optimizer (`OptimizerGeneric`) then iteratively adjusted the variables to find the optimal configuration. Upon completion, we visualized the final system using `system.draw()`, generated updated spot diagrams, and printed the optimized angles. We apply these settings in Section 'Simulation Results' and compare pre- and post-optimization spot diagrams to quantify the separation.

Picomotor Characterization

To translate the optimized model into hardware, we needed to verify that the picomotor-driven mirror mounts could actually reach and stably hold the target tilts predicted by our optimization code. In practice, alignment quality is limited by actuator behavior, so we quantified each motor's step-to-angle calibration, linearity, and hysteresis for the mirrors under control (A and C). This bridges the simulation to the lab by setting realistic step sizes and tolerances for the alignment procedure. The next section details the measurement setup and analysis.

We characterized the picomotors, each with two actuators for yaw and pitch, corresponding to horizontal and vertical angular displacement. The setup used a diode laser and a mirror mounted on a picomotor stage at approximately 45° to reflect the beam onto a distant wall covered with grid paper. The mirror-to-wall distance was precisely measured as 2.221 m with a laser distance measurer, making its uncertainty negligible.

Using the small-angle approximation, the angular deflection θ in radians was related to the spot displacement s on the wall by:

$$\theta = \frac{s}{L} \tag{1}$$

where $L = 2.221$ m. Motors were actuated in 100-step increments, moving the beam by one grid unit, starting from the center and sweeping in both directions. This was repeated for both horizontal and vertical motors, and the displacement data was plotted in Excel.

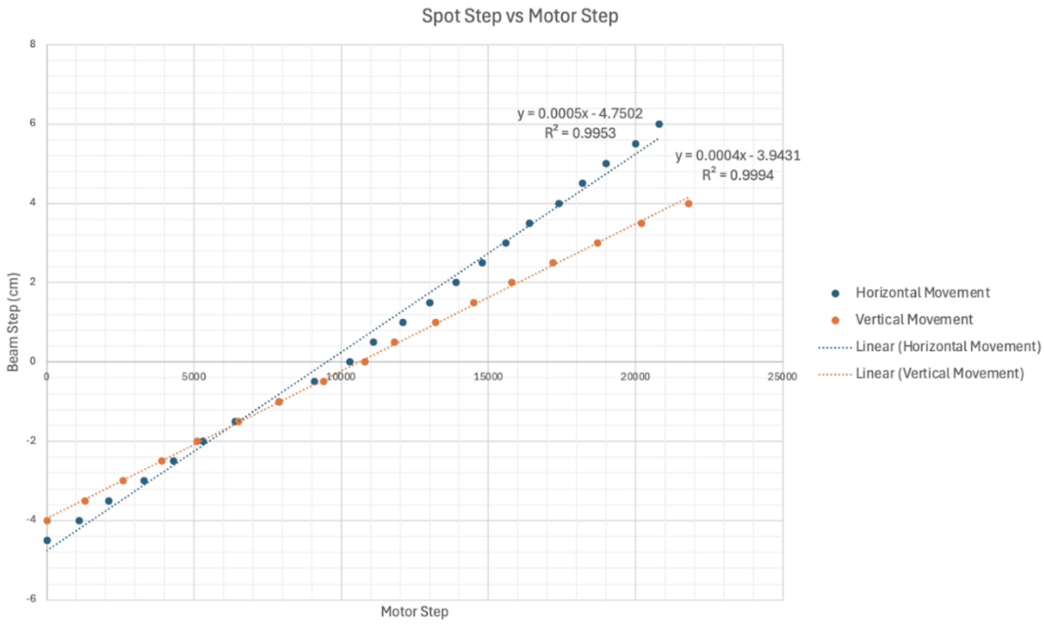

Figure 3: Measured relationship between motor step count and beam displacement for horizontal and vertical picomotor movements

The results from Figure 3 showed different gradients for vertical and horizontal motors. Possible causes include imperfect centering of the horizontal beam, mechanical differences between motors, and slight deviations from linearity due to mirror alignment or approximation limits.

Using equation 1, measurement uncertainty was estimated from the grid paper resolution: ± 1 mm over 2.221 m corresponds to:

$$\Delta\theta = \frac{\Delta s}{L} = \frac{0.001}{2.221} \cdot \frac{180}{\pi} \approx 0.026^\circ$$

Thus, each angular measurement carried an uncertainty of approximately $\pm 0.026^\circ$. Motor position uncertainty was estimated at ± 100 steps.

To investigate the irregularities, we tested for hysteresis by performing large and small displacement sweeps and analyzed the data with a Python script. The script converted displacement to angular deflection, segmented the data by motion direction, and applied Orthogonal Distance Regression (ODR) to account for uncertainties in both axes. We also completed experiments with an alternative starting position for the laser, as well as a modified distance between the mirror and wall.

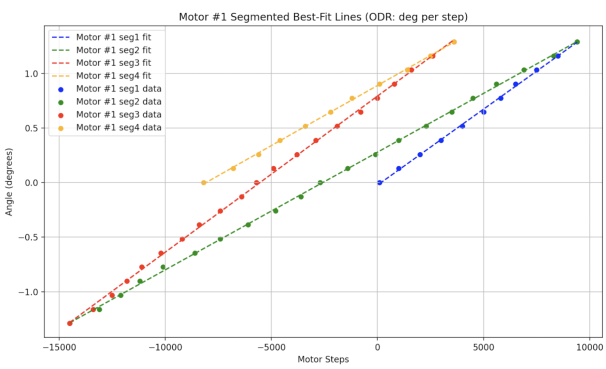

(a) Segmented best-fit analysis of Motor 1 angular displacement versus motor steps, showing linear trends for each motion segment and highlighting potential hysteresis effects.

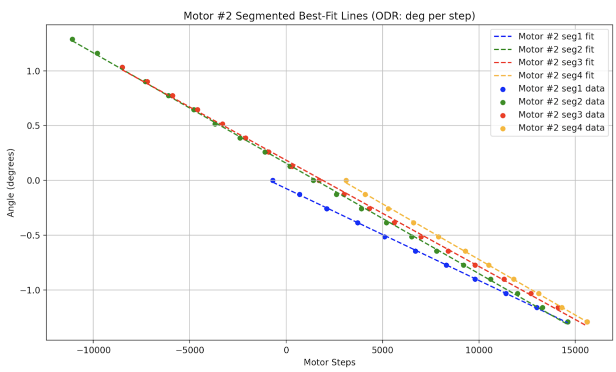

(b) Segmented best-fit analysis of Motor 2 angular displacement versus motor steps, showing linear trends for each motion segment and highlighting potential hysteresis effects.

Figure 4: Comparison of segmented best-fit analysis for Motor 1 and Motor 2.

Table 2: Motor 1 results.

Seg.	Slope (°/step)	Unc. (°/step)	Dir.
1	0.000139	0.000002	Right
2	0.000108	0.000000	Left
3	0.000143	0.000001	Right
4	0.000110	0.000001	Left

Table 3: Motor 2 results.

Seg.	Slope (°/step)	Unc. (°/step)	Dir.
1	-0.000084	0.000001	Up
2	-0.000101	0.000000	Down
3	-0.000097	0.000001	Up
4	-0.000102	0.000001	Down

Rightward and leftward motions yielded consistent slopes within each direction but differed between directions, indicating hysteresis. This directional asymmetry causes the mirror not to return to its exact angular position when reversing motion. The vertical motor showed less discrepancy, likely due to better mechanical centering.

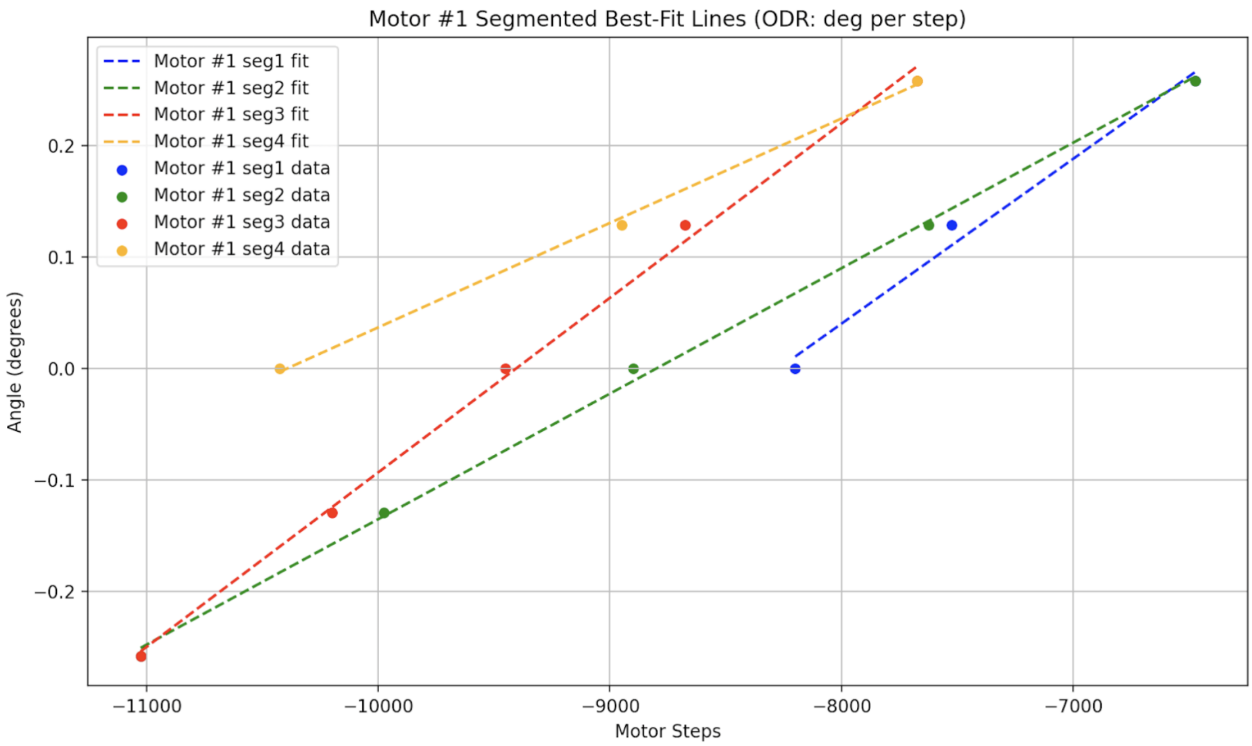

Figure 5: Close-up segmented best-fit analysis of Motor 1, highlighting slope differences between rightward and leftward movements that reveal hysteresis effects and directional asymmetry in angular response.

Table 4: *Close-up Motor 1 results.*

Seg.	Slope (°/step)	Unc. (°/step)	Dir.
1	0.000148	0.000018	Right
2	0.000113	0.000002	Left
3	0.000156	0.000005	Right
4	0.000094	0.000004	Left

In the close-up motor experiment, the asymmetry persisted, with slope magnitudes slightly different from previous trials, suggesting that the initial starting position influences the step-to-angle relationship.

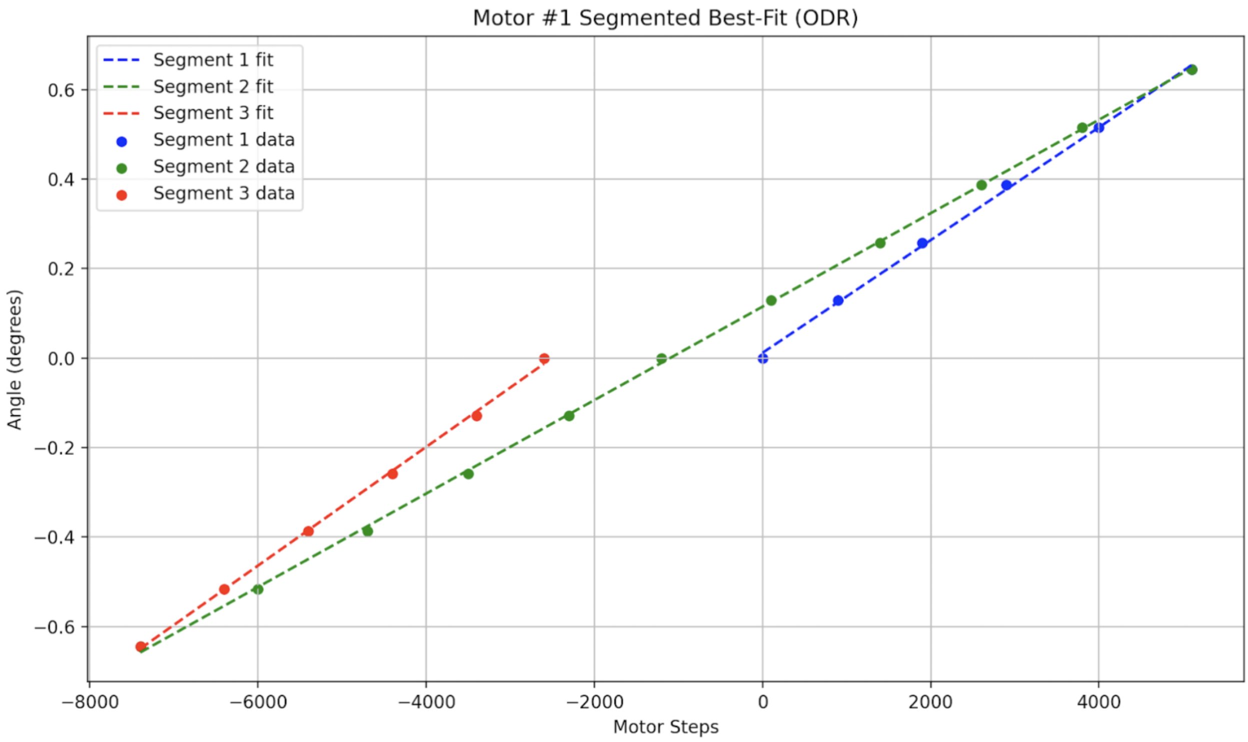

Figure 6: Segmented best-fit analysis of Motor 1 for an alternative central starting position, showing consistent slopes within each movement direction but a clear difference between rightward and leftward motion, suggesting directional dependence in angular displacement.

Table 5: Alternative starting position results for Motor 1.

Seg.	Slope (°/step)	Unc. (°/step)	Dir.
1	0.000126	0.000002	Right
2	0.000104	0.000001	Left
3	0.000133	0.000002	Right

In the alternative starting position experiment, rightward slopes remained larger than leftward, again confirming directional dependence.

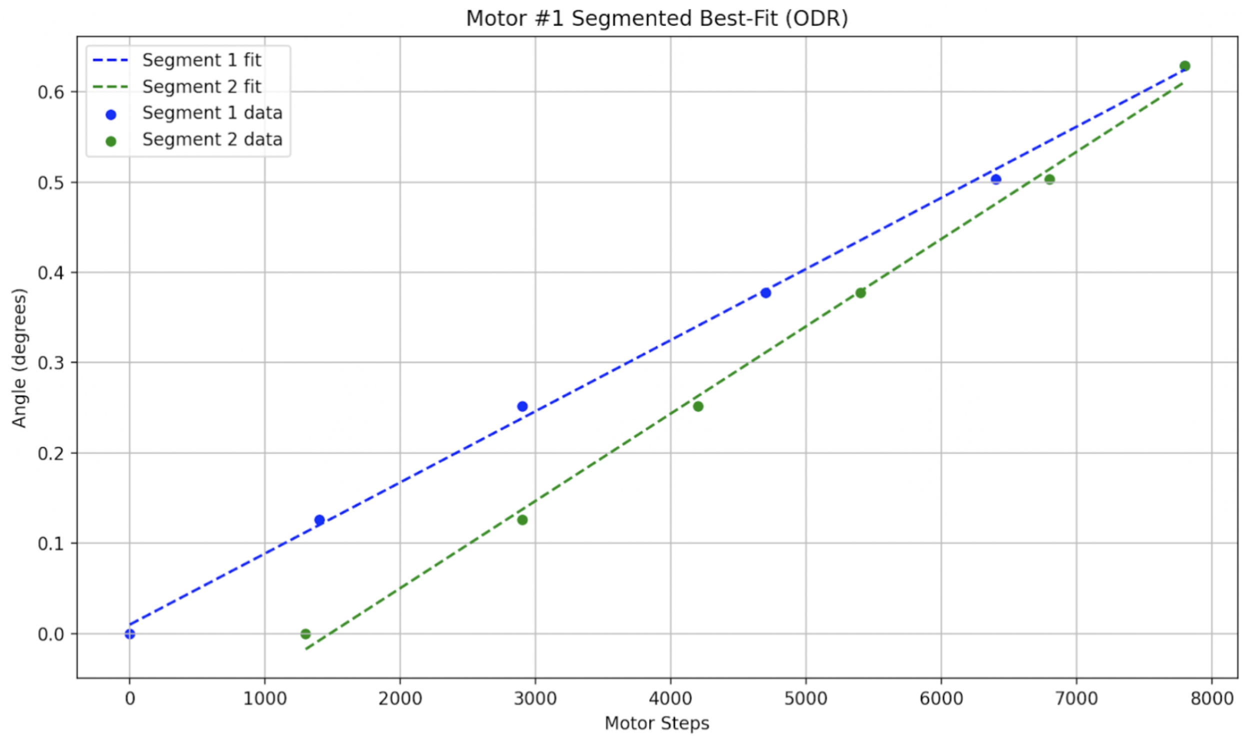

Figure 7: Segmented best-fit analysis showing consistently larger slopes for rightward motion compared to leftward motion, with slope magnitudes differing from previous trials—highlighting the influence of initial starting position on motor behavior.

Table 6: Modified distance test (2.277 m) results for Motor 1.

Seg.	**Slope (°/step)**	**Unc. (°/step)**	**Dir.**
1	0.000079	0.000002	Right
2	0.000097	0.000003	Left

The same directional asymmetry was observed in the modified distance test, with different slope magnitudes compared to previous trials. This dependency on starting position and geometry complicates consistent characterization and highlights the need for a feedback mechanism to correct for drift and directional offsets.

Automation and Feedback Approaches

Due to the inconsistent behavior of the picomotors, we concluded that a closed-loop feedback system would offer a more reliable solution. The idea was to pair an optical optimization algorithm with the motors: the code would determine the optimal beam path, command the motors to move a set number of steps, and then, using feedback, evaluate whether the beam had overshot or undershot the target. However, because both the 365 nm and 121.6 nm beams are extremely sensitive and easily degraded by physical obstructions, we aimed to utilize the small portion of light that leaks through the mirrors (rather than being fully reflected) for non-invasive feedback.

Our proposed design involved placing a quadrant photodiode (QPD) behind the mirror. This sensor would detect the position of the transmitted beam and provide real-time positional feedback via LabVIEW, allowing us to track the beam's impact location across the sensor's four quadrants and make precise adjustments accordingly.

However, when attempting to test this system, we encountered several limitations. The QPD available in the lab was designed specifically for pulsed laser systems, such as the Lyman-alpha setup, and did not function with the continuous-wave diode used in the previous setup. Moreover, even during its initial application in the Lyman-alpha experiment, the sensor had proven to be unreliable, operating at the 50 Hz repetition rate of the laser after an upgrade. Due to these hardware constraints and their unreliability, we were unable to perform a preliminary validation of the feedback concept. Consequently, we determined that implementing a feedback system using the existing sensor would not be a viable solution at this time.

Alternative Alignment Solutions

Since the picomotors' reproducibility proved to be unreliable, we sought an alternative approach to simplify the alignment and calibration process of the optical system. To address this, we decided to incorporate irises mounted on translation stages as passive alignment aids. The initial intention was to utilize the optimization code to generate an ideal beam path. With this theoretical trajectory known, we could then strategically place irises along the expected beam path and manually adjust the mirrors until the beam passed cleanly through each aperture.

This method removes the need for fine motor adjustments by providing a physical visual cue for beam alignment. The proposed setup involves mounting two irises on vertical translation stages that could be adjusted using micrometers. Each iris is fixed on a translation stage, constraining its horizontal position while allowing for vertical adjustment only. The configuration would appear as follows:

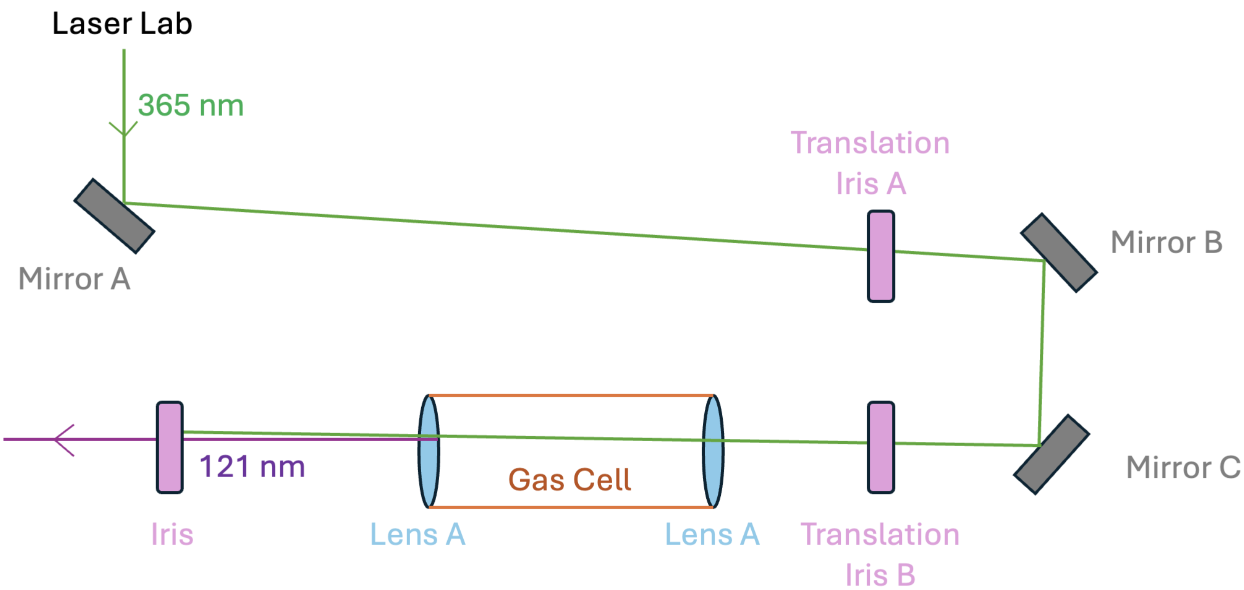

Figure 8: Updated optical setup with translation-mounted irises for precise beam alignment and spatial filtering of the 365 nm and 121.6 nm beams.

To implement this setup, we first had to extend the existing optical system, as there was no available space to mount the translation stages. To ensure proper laser containment and adhere to safety protocols, we decided to enclose the extended section with blackout boards, forming a light-tight box. The enclosure was designed with a removable lid to allow easy access during adjustments.

Integrating the extension proved challenging, requiring the careful repositioning of several components within the existing ALPHA setup. This involved relocating an air manifold, removing an unused laser beamline, and rerouting hoses connected to the atom trap. Additional support beams were installed to secure the new breadboard in place. Once the breadboard was mounted, we installed the translation stages with their irises, along with Mirrors 2 and 3 of the setup. A new survey was then carried out to record the updated system dimensions. Using the violet alignment laser, we verified the correct placement of all optical elements before updating the system parameters in our optimization code to reflect the revised geometry.

Table 7: Optimized Optical Path Parameters for VUV Generation Setup

Component/Section	**Details**
Beam Entry Point	Enters at Mirror A
Mirror A to Translation Iris A	Distance: 153 cm (center optics, free air)
Translation Iris A to Mirror B	Distance: 16 cm
Mirror B	Flat mirror, Diameter: 2.5 cm
Mirror B to Mirror C	Distance: 11 cm (free space)
Mirror C	Flat mirror, Diameter: 2.5 cm
Mirror C to Translation Iris B	Distance: 12 cm
Translation Iris B to Lens A	Distance: 50 cm
Lens A	Focal Length: 300 mm
Lens A to Lens B	Distance: 48 cm (enclosing gas cell) Gas Type: Argon/Krypton Gas Pressure: $\sim$2300 $\pm$ 1 Torr
Lens B	Focal Length: 150 mm
Lens B to Iris	Distance: 96 cm

Simulation Results

To establish a baseline, we first aligned the 365 nm and 121.6 nm beams to be co-linear and centered through the optics and irises, producing a single overlapped spot at the image plane. We then used the Optiland model to seek a small, controlled angular retuning that would keep the beam on the image plane while introducing a clean spatial separation between the two wavelengths at the final iris (so the 365 nm could be blocked while the 121.6 nm passed).

Before optimization, the mirror angles were $A = 49.5208°$, $B = 49.4000°$, and $C = 45.0449°$, producing a centered, overlapped beam path. These parameters centered the initial beam path. After optimization, mirror B remained unchanged at 49.4000° (non-motorized), while mirror A and mirror C shifted slightly to 49.5671° and 45.0070° (Table 8). The simulation also indicated small changes in the vertical alignment of the irises (z-axis positions). Iris A shifted from 339 mm to 342 mm, and Iris B from 482 mm to 479 mm (Table 9). These position updates inform fine adjustments on the translation stages to replicate the simulated separation in the physical setup. The beam path optimization and separation can be observed in Figures 9 and 10.

Table 8: Mirror rotation parameters before and after optimization.

Mirror	**Before (°)**	**After (°)**
A	49.5208	49.5671
B	49.4000	49.4000
C	45.0449	45.0070

Table 9: *Iris z-axis positions before and after optimization.*

Iris	Before (mm)	After (mm)
A	339	342
B	482	479

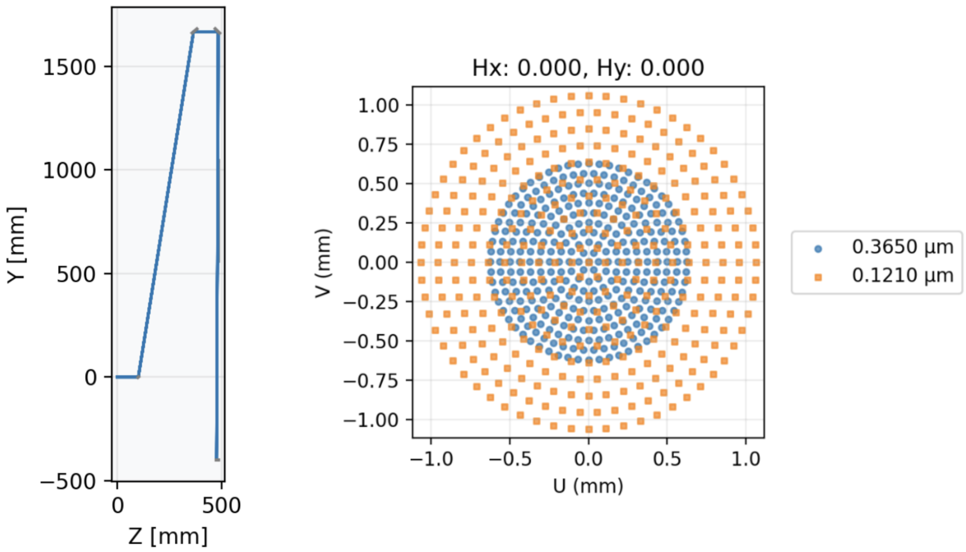

Figure 9: Simulation output showing the pre-optimization beam path and the spot diagram at the last iris. The 365 nm and 121.6 nm beams are overlapped and centered, indicating precise initial alignment before further tuning.

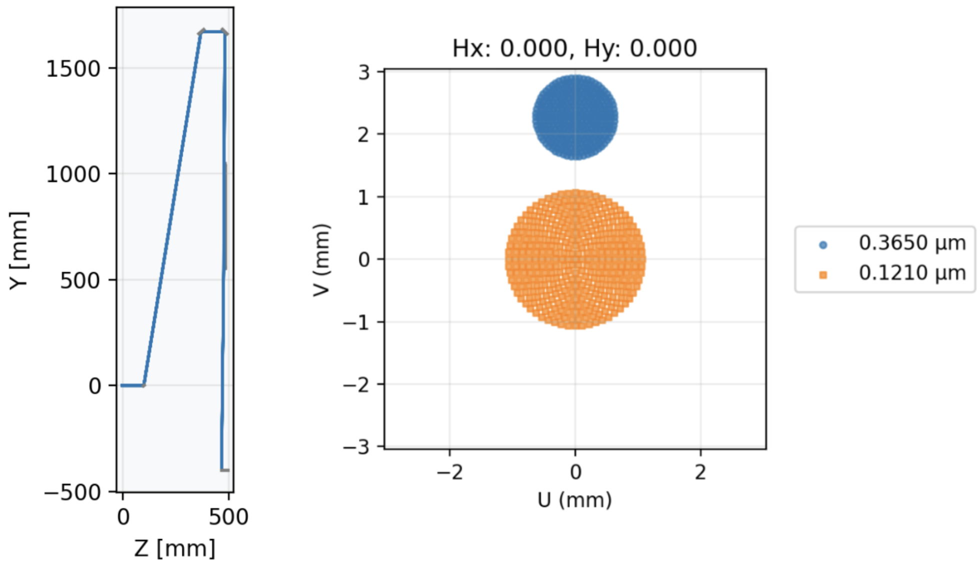

Figure 10: Post-optimization simulation showing the beam path and spot diagram at the last iris. The 365 nm and 121.6 nm beams are now spatially separated, achieving the desired displacement for downstream alignment and diagnostics.

Conclusion

This project successfully developed and optimized a VUV laser alignment system for antihydrogen cooling in the ALPHA experiment. Through detailed optical surveying, ray-tracing simulation, and iterative alignment strategies, we improved the reproducibility and efficiency of the third-harmonic generation process for producing 121.6 nm light. Picomotor characterization revealed nonlinearities and hysteresis, highlighting limitations for automation and motivating the adoption of a passive alignment method using translation-mounted irises. This approach streamlined beam alignment while preserving precision, and the updated optical model provides a robust framework for future closed-loop feedback integration. The methodology established here strengthens the reliability of the Lyman-alpha generation system, supporting ALPHA's long-term goal of high-precision antihydrogen spectroscopy and cooling.

References

[1] A. Riotto and M. Trodden, “Recent progress in baryogenesis,” *Annual Review of Nuclear and Particle Science*, vol. 49, pp. 35–75, 1999.

[2] S. Maury, “The antiproton decelerator: Ad,” *Hyperfine Interactions*, vol. 109, no. 1–4, pp. 43–52, 1997.

[3] T. Eriksson, S. Maury, S. Bousson, F. Butin, V. Chohan, K. Hanke *et al.*, “Elena: Extra low energy antiproton,” *Hyperfine Interactions*, vol. 240, no. 1, p. 8, 2019.

[4] G. B. Andresen *et al.*, “Trapped antihydrogen,” *Nature*, vol. 468, pp. 673–676, 2010.

[5] C. Amole *et al.*, “Resonant quantum transitions in trapped antihydrogen atoms,” *Nature*, vol. 483, pp. 439–443, 2012.

[6] M. Ahmadi *et al.*, “Observation of the 1s–2s transition in trapped antihydrogen,” *Nature*, vol. 541, pp. 506–510, 2017.

[7] G. B. Andresen *et al.*, “Antimatter confinement in a penning-malmberg trap,” *Physics Letters B*, vol. 685, pp. 141–145, 2010.

[8] G. Gabrielse *et al.*, “First capture of antihydrogen atoms,” *Physical Review Letters*, vol. 89, p. 213401, 2002.

[9] M. Ahmadi *et al.*, “Laser cooling of antihydrogen atoms,” *Nature*, vol. 592, pp. 35–42, 2021.

[10] G. B. Andresen *et al.*, “Laser cooling of antihydrogen,” *Nature Communications*, vol. 4, p. 1785, 2013.

[11] P. H. Donnan, M. C. Fujiwara, and F. Robicheaux, “Antihydrogen laser physics,” *Journal of Physics B: Atomic, Molecular and Optical Physics*, vol. 46, no. 2, p. 025302, 2013.

[12] A. Evans, “Laser cooling of antihydrogen for alpha-g,” Ph.D. dissertation, University of Calgary, 2022.